Ore Geology Reviews 137 (2021) 104306

Contents lists available at ScienceDirect

Ore Geology Reviews

journal homepage: www.elsevier.com/locate/oregeorev

Reflection seismic imaging to unravel subsurface geological structures of the Zinkgruvan mining area, central Sweden

Alba Gil [a,*], Alireza Malehmir [a,*], Stefan Buske [b], Juan Alcalde [c], Puy Ayarza [d], Yesenia Martínez [c], Louise Lindskog [e], Bill Spicer [f], Ramon Carbonell [c], Dirk Orlowsky [g], Jorge Carriedo [f], Anja Hagerud [e]

[a] Department of Earth Sciences, Uppsala University, Uppsala, Sweden
[b] Institute of Geophysics and Geoinformatics, Technische Universität Bergakademie Freiberg, Freiberg, Germany
[c] Geosciences Barcelona (Geo3Bcn-CSIC), Barcelona, Spain
[d] Department of Geology, University of Salamanca, Salamanca, Spain
[e] Zinkgruvan Mining AB, Zinkgruvan, Sweden
[f] Lundin Mining Corporation, Toronto, Canada
[g] DMT GmbH & Co, Essen, Germany

ARTICLE INFO

Keywords:
Reflection seismic
Mineral exploration
Modeling
Zinkgruvan

ABSTRACT

The Zinkgruvan mining area is located on the south-eastern part of the Bergslagen district, one of the three major mineral producing regions in Sweden. In this study, we present the results from three (P1, P2 and P8) reflection seismic profiles each approximately 3000 m-long crossing the Zinkgruvan Zn-Pb-Ag-(Cu) mining area. P1 was acquired using cabled geophones with 10 m receiver and source interval and crossed major geological features. The other two profiles (P2 and P8) were acquired by wireless recorders with 20 m receiver and 10 m source interval and ran perpendicular to P1. Through a special data processing workflow adapted to this dataset, good quality seismic sections were obtained along these profiles, although a high noise level due to high voltage electric power lines was present. The interpretations were constrained by (1) seismic P-wave velocity and density data from a series of downhole logging measurements, (2) 3D forward reflection traveltime modelling in both pre- and post-stack domains, and (3) other geophysical and geological observations available from the site. Despite the notably complex geology, the processed seismic sections clearly reveal a series of horizontal to gently dipping reflections associated with known geological formations. Results indicate that most structures and lithological contacts dip or plunge to the northeast, including the targeted Zinkgruvan Formation. The results from this seismic survey are encouraging regarding the potential of the seismic method for base-metal exploration in Sweden and in particular in the Bergslagen district. It shows the high resolving power of the reflection seismic methods for imaging complex geological structures in a cost-effective and environmentally-friendly way.

1. Introduction

Mineral resources are used in larger quantities than ever before (Zepf et al., 2014; Schmidt, 2019) as they are fundamental to our modern society. Population growth, together with an overall improvement of living standards, greater levels of environmental awareness and energy transition towards green technologies, result in global increase in demand for sustainable mineral resources. Exploration is the first step in the mineral resource cycle and the so-called value chain. Supply of raw materials to address the increased demand is essential for the full functionality of this chain. Mineral exploration, however, is more challenging these days. On one hand, the majority of giant deposits at shallow depths (<500 m) have already been found and mined out, and the industry is moving towards deeper and more complex mineral systems (Humphreys, 2018). On the other hand, the mining sector needs time-saving, cost-effective, environmentally friendly and socially acceptable techniques to ensure sustainable access to mineral resources. To be successful in exploration, a better understanding of the geological structures and the evolution (tectonic framework) of a mining area is necessary. Several studies have shown that geophysical methods, such as

* Corresponding authors.
E-mail addresses: alba.gil@geo.uu.se, albgil@gmail.com (A. Gil), Alireza.Malehmir@geo.uu.se (A. Malehmir).

https://doi.org/10.1016/j.oregeorev.2021.104306
Received 22 April 2020; Received in revised form 20 May 2021; Accepted 15 June 2021
Available online 18 June 2021

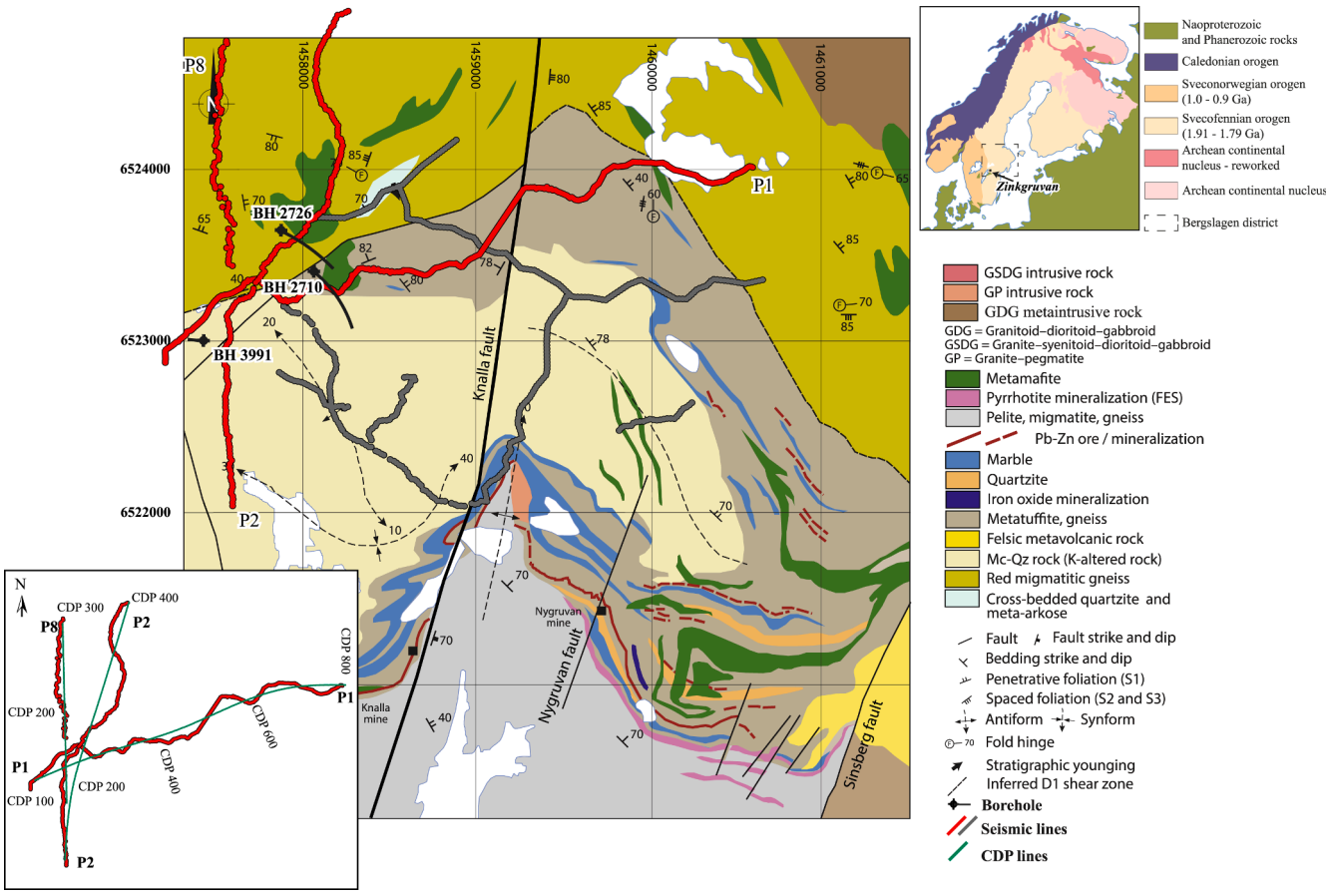

Fig. 1. Geological bedrock map of the Zinkgruvan mining area (modified from Stephens et al., 2009; Jansson et al., 2017) showing the location of the seismic profiles (grey and red lines), major structures mapped in the area and boreholes shown in this study. The focus of this study is profiles P1, P2 and P8 that are shown in red (see inset figure). Note parts of P2 and P8 overlap.

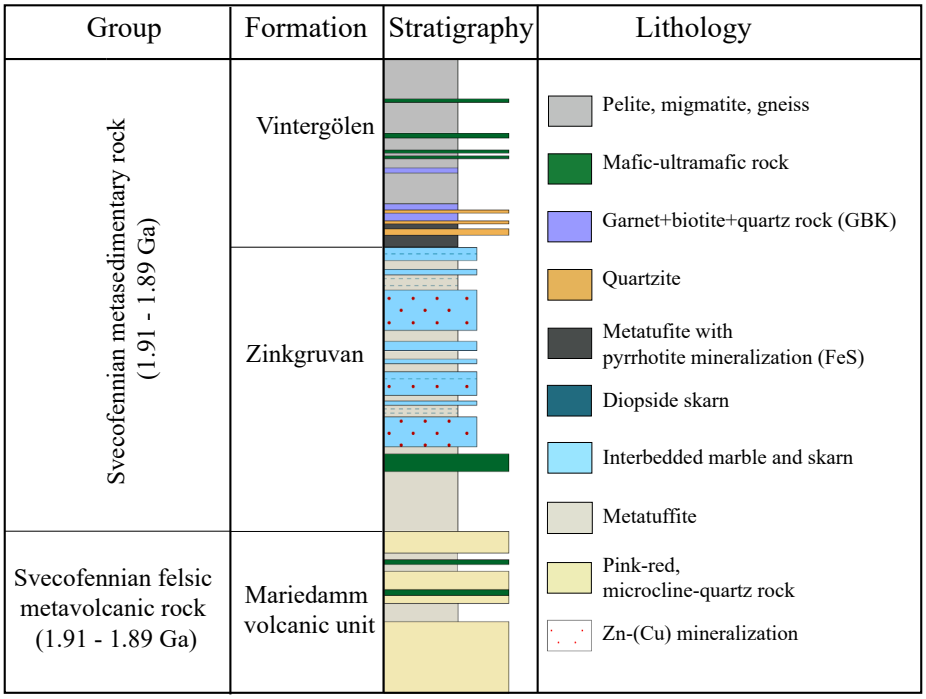

Fig. 2. Regional stratigraphic column of the Zinkgruvan mining area. The column is based on Jansson et al. (2017, 2018) and drill holes 2726 and 3391 (Fig. 1). The stratiform Zn-Pb-Ag-(Cu) mineralization is hosted in the Zinkgruvan Formation. However, this regional stratigraphic column is not fully representative for the Zinkgruvan Formation since it is based on only two drill holes that do not intersect the main ore-baring horizon.

Fig. 3. Seismic source and various receiver types used during the Zinkgruvan acquisition (November 2018). (a) Arial photo of the 32 t vibrator along profile P1. (b) SERCEL 428 cabled system, (c) CUBE wireless data recorders, and (d) Sercel UNITE wireless 1C recorders where possible geophones were planted in the bedrock to obtain higher S/N data.

Table 1
Zinkgruvan seismic data acquisition parameters (Fall 2018) of the main profiles (P1, P2 and P8) discussed in this study.

Profiles parameter	P1	P2	P8
Type	2D crooked line		2D straight line (along a power line)
Data recorder	SERCEL 428UL FDU	Wireless CUBES	Wireless UNITE
No. of active receivers	425-1C	165-1C	138-1C
Receiver spacing	10 *m*	20 *m*	20 *m*
Geophone	28 Hz	4.5 Hz	Mixed 4.5 Hz (66 rec. south) and 10 Hz (72 rec. north)
Source	TU Bergakademie Freiberg 32 t vibrator		
Sweep parameters	10–150 Hz, 17 s long, 3 sweeps per shot location		
No. of source position	243	288	129
Source spacing	10 *m*	10 *m*	10 *m*
Profile length	3500 *m*	3000 *m*	2800 *m*
Nominal fold	212	165	138
Sampling interval	1 ms	1.25 ms	1.25 ms south 1 ms north

seismics and electromagnetics, can provide important information about geological structures hosting mineral deposits. Reflection seismics has the potential to support mineral exploration either by directly imaging mineral deposits at depth (Schmidt, 1959; Kehrman, 1980; Juhlin et al., 1991; Eaton et al., 2003 and the references therein; Malehmir and Bellefleur, 2010; Malehmir et al., 2012a; and Malehmir et al., 2020 and the references therein; Ahmadi et al., 2013; Buske et al., 2015 and the references therein; Singh et al., 2019) or by defining faults and structures that control or host mineral deposits (Gupta, 1971; Adam et al., 1992; Milkereit and Eaton, 1998; Manzi et al., 2012; and Manzi et al., 2019; Alaei and Torabi, 2017; Malehmir et al., 2017a; Donoso et al., 2019; Markovic et al., 2019). Nowadays, with the advancement in data acquisition and processing technologies, high-resolution seismic surveys in mining environments have been effective in imaging even complex geological structures (Ruskey, 1981; Wu et al., 1995; Tryggvason et al., 2006; Malehmir et al., 2012b, 2018; Zhao et al., 2018).

On this front, and facing an up-scaling challenge, the EIT Raw-Materials funded project SIT4ME (Seismic Imaging Techniques for Mineral Exploration) was launched involving several European Institutions. As part of this project a dense multi-method seismic dataset was acquired in November 2018 in the Zinkgruvan mining area at the Bergslagen mineral district of Sweden, which hosts one of the largest volcanic-hosted massive sulphide (VMS) deposits in the country.

The main objectives of this study are to address: (1) how seismic imaging can contribute to improve the understanding of the subsurface

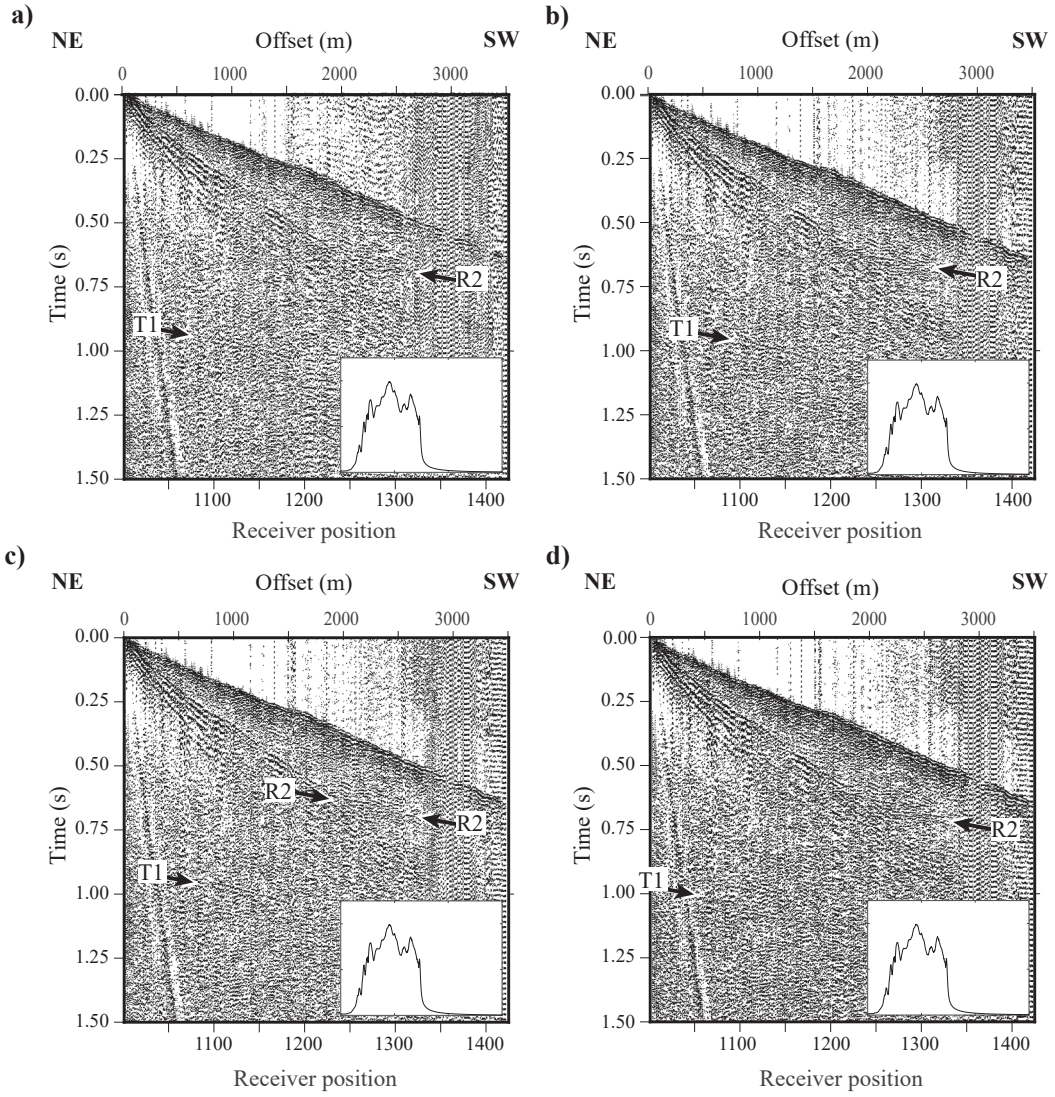

Fig. 4. Example shot gather at the same position but using four different length vibrator sweeps. Sweep length (a) 16 s, (b) 17 s, (c) 18 s and (d) 20 s. Black arrows show reflections (R2 and T1) observed during the source parameter test. Encapsulated figures show the corresponding amplitude spectrum (normalised to one shown for 0–300 Hz) for each sweep length. A sweep frequency bandwidth of 10–150 Hz was used in all these tests. A sweep length of 17 s was considered as optimum for the survey.

geological structures in this complex setting and (2) how effectively seismic reflections can be correlated to local geological structures that are mapped on surface geological map and borehole data. Apart from a dedicated survey setup, our interpretation benefits from 3D reflection traveltime modelling performed on both shot gather and unmigrated stacked sections. This helps to better control on the 2D profiles crookedness and potential out-of-the-plane features (Ayarza et al., 2000; Dehghannejad et al., 2010). This study provides important constraints on the structure of the area by linking some near-surface reflections to outcropping rock units (Jansson et al., 2017, 2018) and to downhole logging data. We show how the seismic data can shed light on key geological structures that host the mineralization and may define regions where deep targeting is achievable in future exploration programs.

2. Geological background

2.1. Bergslagen region

Zinkgruvan is located in the Bergslagen mineral district of the Fennoscandian Shield, known for its vast and diverse mineral resources and complex tectonic history (Gaál and Gorbatschev, 1987; Stephens et al., 2009; Beunk and Kuipers, 2012; Buntin et al., 2019). Bergslagen (central Sweden) lies at the south-western part of the Svecofennian (or Svecokarelian) orogen and is well-known for its over 6000 mineralization occurrences and prospects. Fe-oxide deposits make up the majority of the metallic mineral deposits, whereas polymetallic (primarily massive sulphides) deposits are subordinate (Allen et al., 2003). Three polymetallic sulphide mines are currently in operation in the Bergslagen

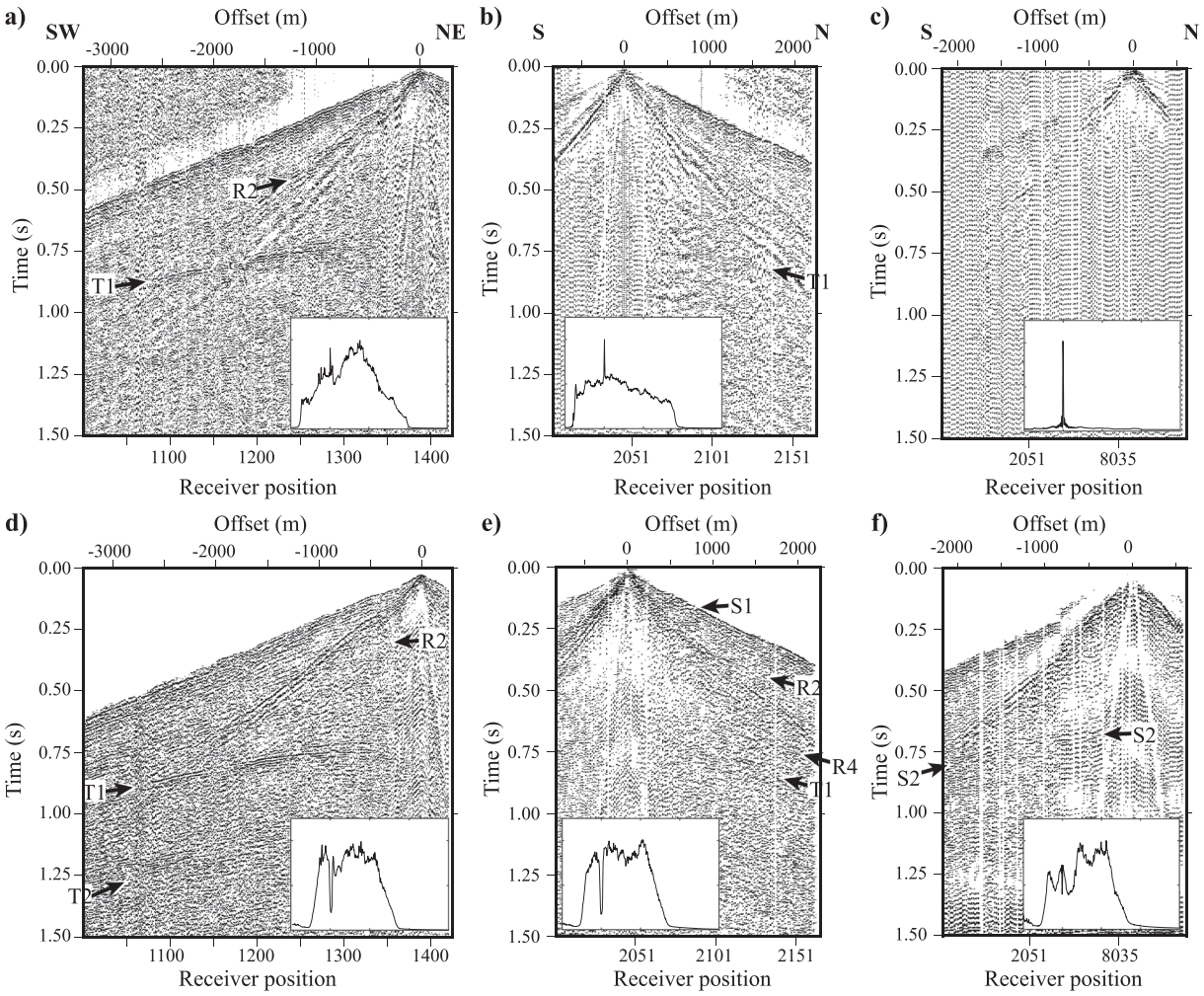

Fig. 5. Three shot gather examples from P1, P2 and P8, with their corresponding frequency spectrum normalised to one and shown for 0–200 Hz. (a–c) Raw and (d–f) processed shot gathers highlighting clear reflections marked by the black arrows. Note the dominant 50-Hz noise recorded in all of the shot gathers. Along P8, the 50 Hz noise is much more sever, as this profile is adjacent to a major power line.

district: the Zn-Pb-Ag-(Cu-Au) deposit of Garpenberg, the Zn-Pb-Ag deposit of Lovisagruvan, and the Zn-Pb-Ag- and Cu deposit of Zinkgruvan. The latter is the focus of our study.

Most surface rocks in the Bergslagen mineral district are of Svecofennian age (1.91–1.79 Ga). However, the westernmost part is situated in the frontal part of the Sveconorwegian orogen (1.0–0.9 Ga) (Stephens et al., 2009; Fig. 1). Beunk and Kuipers (2012) defined four successive tectonic phases that have deformed the Bergslagen region. These are: (1) continental rifting associated with bimodal magmatism in continental back-arc basins, associated to 1.91–1.89 Ga (D_1), (2) closure of the rift(s) by upright tight to isoclinal folds (D_2), stage completed around 1.86 Ga, (3) renewed rifting (D_3) with deposition of argillites, conglomerates and submarine basalts in restricted rift basins, estimated between 1.87 and 1.84 Ga, and (4) intense buckling and folding of west Bergslagen along variably but generally steeply plunging folds, associated to 1.82–1.79 Ga (D_4). The southern part of Bergslagen presents prominent dolerite dykes as wide as 1000 m that are visible on the surface. These dykes have a strike of WNW-ESE, and a strong dip component (60°), as they have been inferred from airborne magnetic data (Stephens et al., 2009). Beunk and Kuipers (2012) associated the dolerite dykes to an extensional event between the D2 and D4 phases (1.86–1.85 Ga).

2.2. Zinkgruvan mining area

Zinkgruvan Mining AB, a subsidiary company of Lundin Mining Corporation, mines the deposit. Zinkgruvan is currently the southernmost underground mine in Sweden and produces concentrates of Zn, Pb and Cu. The deposit has previously been referred to as "Åmmeberg-type" (Geijer, 1917), and more recently as "stratiform ash-siltstone-hosted Zn-Pb-Ag sulphide deposit (SAS-type)" (Allen et al., 1996). Like most metallic deposits in the district, it is spatially associated with hydrothermally altered felsic volcanic rocks (rhyolitic to dacitic), marble, skarn and metasedimentary rocks.

The stratigraphic setting of the Zinkgruvan deposit (Fig. 2) has been described in detail by Hedström et al. (1989), Allen et al. (1996) and Kumpulainen et al. (1996), among others. Jansson et al. (2017) defined the Zinkgruvan Formation as the region compressed between the 'Mariedamm volcanic unit' and the 'Vintergölen Formation' of the informally referred as the 'Emme Group' (Hedström et al., 1989; Kumpulainen et al., 1996). The Zinkgruvan Formation is a succession of grey, mainly fine-grained, biotite-bearing quartz-feldspathic rocks (the metatuffites unit), calc-silicate units and marble (Fig. 2). The stratiform Zn-Pb-Ag-(Cu) mineralization is hosted in the dolomite marble of the Zinkgruvan Formation (Jansson et al., 2017).

The tectonic setting of the Zinkgruvan deposit is complex as it is characterised by a multiphase deformation history (Fig. 1). Repeated deformation during the Svecofennian orogeny includes later N-S folding defining a series of vertical folds that affect previous E-W structures (Hedström et al., 1989; Jansson et al., 2017). Due to stratigraphic inversion, youngest stratigraphic units are located mainly southwards of

Table 2
Processing steps for the reflection seismic datasets of P1, P2 and P8, Zinkgruvan.

1	Prepare SEGY-files (vertical stack)
2	Cross-correlation (theoretical sweeps)
3	Geometry set-up:
	P1: Wiggly CDP 5 m bin size
	P2: Wiggly CDP 10 m bin size
	P8: Linear CDP 10 m bin size
4	Picking first arrivals
5	Median filter
6	Refraction and elevation correction:
	P1: Datum: 190 m, replacement velocity 5500 m/s
	P2: Datum: 185 m, replacement velocity 5500 m/s
	P8: Datum: 190 m, replacement velocity 5500 m/s
7	Trace editing
8	Remove 50 Hz noise:
	Notch filter at 50 Hz
9	Band-pass filter: 10–30-120–150 Hz
10	Spectral equalization: 20–40-100–140 Hz
11	Remove first arrival energy
12	Residual statics (looped)
13	Velocity analysis
14	NMO corrections:
	50% stretch mute
15	Stack
16	Post-stack coherency enhancement (Fx-deconvolution)
17	Migration:
	Finite-difference using a constant velocity 6000 m/s
18	Time-to-depth conversion using 6000 m/s

the mine. Besides folding, the area is also affected by mainly left lateral, NNE-SSW trending strike slip faults, all showing a northward displacement of the eastern limb. Due to the prominent Knalla fault, which cuts across the area, the mining area is divided into two large blocks, the Knallagruvan in the west and the Nygruvan in the east (Fig. 1).

3. Data acquisition

In November 2018, a dense seismic dataset was acquired in the Zinkgruvan mining area (Fig. 1) in a joint collaborative approach among Swedish, Spanish and German Institutes under the SIT4ME project. A dense array of 2D profiles in an area of approximately 6 km^2, crossing habitant areas and forest, was acquired using a 32 t seismic vibrator provided by TU Bergakademie Freiberg (Fig. 3a). Signal penetration was generally good for deep imaging in such a noisy mining environment. Approximately 1300 receiver positions (10–20 m apart), using different types of recorders (Fig. 3b–d), with a variation of recording parameters, and 950 source positions were surveyed. As the main objective was to cover as large area as possible, and considering the limited number of receivers available for this study, a 20 m receiver spacing was used for all the seismic profiles, with the exception of profile P1 that had a 10 m receiver spacing. Due to the great number of receivers needed for the survey, and the limited number of geophones with similar natural frequency, we were on the necessity to use receivers with geophones of different natural frequencies and with different recording parameters (Table 1). Therefore, a combination of geophones with different frequencies were used, where the geophones with higher natural frequency (28 Hz) were used along P1, and consequently compensated with the 10 m receiver spacing along this profile. For P2 and P8 lines, a lower natural frequency (4.5–10 Hz) and a receiver spacing of 20 m was used (Table 1). Each source point consisted of three linear 10–150 Hz upsweeps and a sweep length of 17 s. The spurious frequency of the geophones is 160–180 Hz (according to their manufacturers) and this is consistent with the upper sweep frequency (150 Hz) used in the survey. Sweep parameters were chosen after a careful study prior to the main survey and will be discussed later in the paper. Table 1 lists the main acquisition parameters of the seismic survey.

The profiles were designed, where logistically possible, to be perpendicular to the main geological structures so some key lithological-structural boundaries (e.g., Zinkgruvan Formation) could be imaged. Shot points and receivers were positioned along available forest tracks resulting in a crooked geometry for some of the profiles (Fig. 1). For safety purposes, source locations in the vicinity of buildings and national roads had to be skipped. While 10 profiles were acquired (named P1–P10), this work focuses on the data obtained from P1, P2 and P8 due to the good reflectivity featured, essential to study key geological structures of the surveyed area.

P1, a NE-SW trending 3500 m-long seismic profile, extends from Isåsen to Dalby faults, and crosses over the main NS folding and the Knalla fault (Fig. 1). A fixed spread of 425 active/live channels formed this profile. 28 Hz vertical geophones (Fig. 3a, b) at 10 m spacing were setup along this profile with the main aim to allow live data quality control while the data acquisition was progressing along all other profiles, as it will be shown later. Along P2 (ca. 3000 m-long) and P8 (ca. 2800 m-long), 165 and 138 wireless recorders were used, respectively. For P2, 4.5 Hz vertical-component geophones (Fig. 3c) were used. P8 used 72 vertical-component 10 Hz geophones on the NS continuation of P2 (Figs. 1 and 3d) forming a rather straight NS profile. Both P2 and P8 had 20 m receiver spacing. Data were recorded at 1 ms sampling interval along P1 and P8, and 1.25 ms sampling interval along P2, due to the sensor used for this line (Table 1). The latter data along P2 were later resampled to 1 ms to be able to merge them with the data from the northern portion of P8.

Almost all receiver positions were accurately surveyed using a real-time kinematic DGPS (Differential Global Positioning System) device. However, at places where good quality GPS signal was not available (e.g., in dense forests), the Swedish national LiDAR (light detection and ranging) database was used for determining the elevation. The dense forest or vegetated areas can particularly be troublesome when measuring the elevation of the receiver points, due to the low quality (scattering issues) GPS signal reception. However, a comparison between surveyed positions and LiDAR data was done for quality control estimations of elevation. Errors were found to be less than 10 cm even in forests and densely vegetated places.

3.1. Sweep parameter tests

High-resolution imaging is essential to delineate most geological structures and to take advantage of fine-scale geological knowledge in mining areas. Designing a high-resolution survey implies careful consideration of receiver spacing, fold-offset coverage, source type and frequencies emanated to study the subsurface. All of them are key parameters that depend on the goal of the investigation. In order to choose the optimum seismic source, we first performed a test along P1 to compare a Bobcat-mounted 500-kg drophammer (Urosevic et al., 2009; Place et al., 2015; Malehmir et al., 2017b) with a 32 t seismic vibrator. After a few shots at the same position, it was clear that the drophammer was too weak in this area, as the signal did not reach even half of the spread judged from the quality of the first breaks. The vibrator truck, however, showed a much stronger response and its energy was recorded in the entire spread (of ca. 4000 m), as demonstrated by the quality of the first breaks.

After this initial comparison, the source parameter tests focused on the frequency ranges and sweep lengths of the vibrator. While the source is capable of operating from low (e.g., 7 Hz) to high (e.g., 250 Hz) frequencies, the large number of survey days and the geophones natural frequency (10 Hz) led us to choose sweep frequencies between 10 and 150 Hz. Tests, using 60–70% of the vibrator drive force and higher frequencies (up to 180 Hz), were also done. However, the main focus was put on the sweep length. Four different sweep lengths (i.e., 16, 17, 18 and 20 s) were tried and compared with each other. Fig. 4 shows this comparison after cross-correlation with the theoretical sweeps.

While the four sweeps appear to provide a similar image, a careful look at the first breaks and at two reflections (R2 and T1) helped to decide which sweep length was optimal for the survey. The 17 s sweep

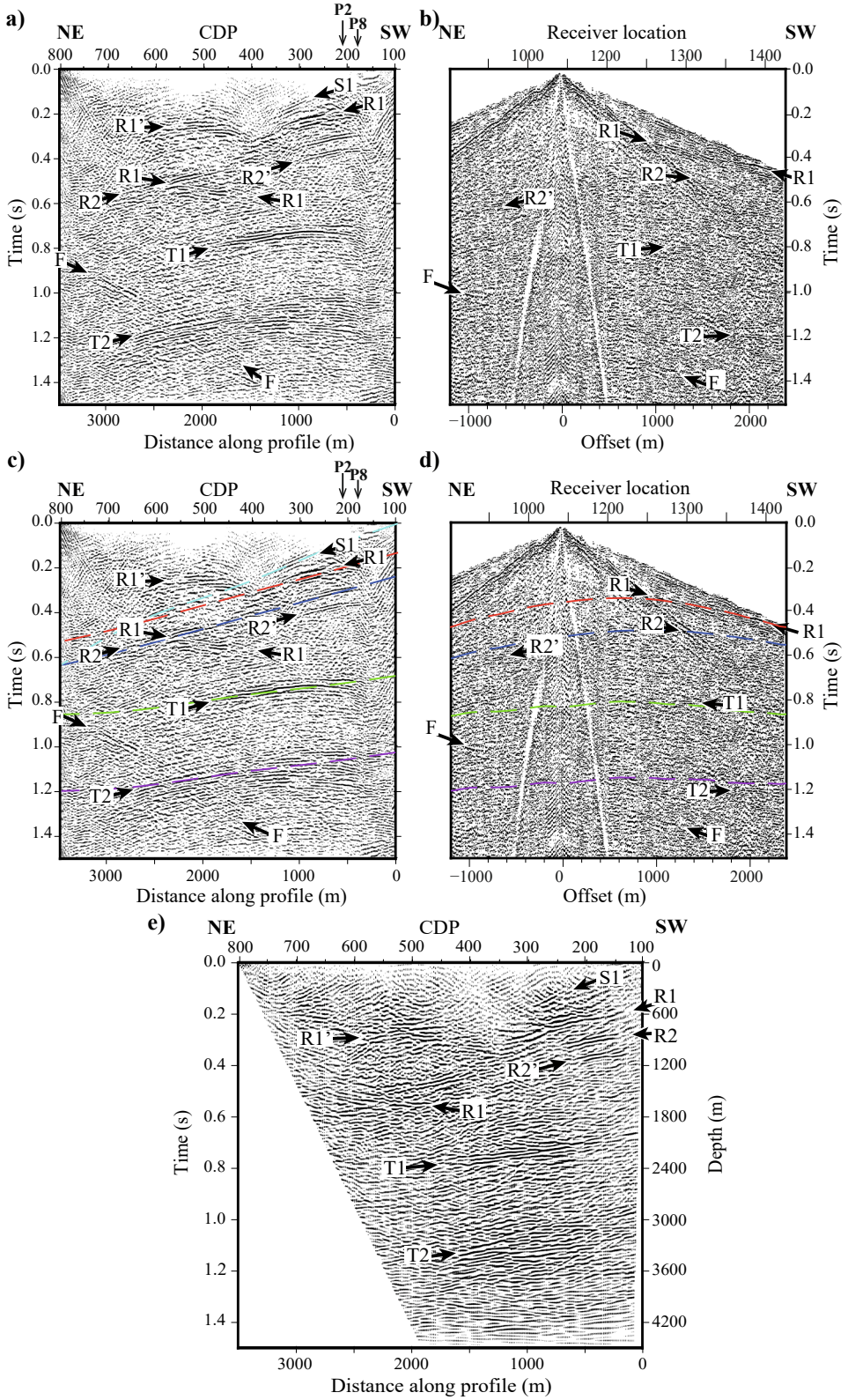

Fig. 6. (a) Unmigrated stacked section and (b) example of a processed shot gather along P1. Traveltimes calculated using the 3D reflection traveltime modelling on (c) the unmigrated stacked section and (d) the shot gather. The modelled traveltimes for reflections S1, R1-R2 and T1-T2 match the observed traveltimes both in the shot gather and the stacked section. (e) Migrated and time-to-depth converted section of P1.

length shows a sharper R2 reflection and good signal penetration at far offsets. The sweep length of 18 s was also judged to be suitable, particularly when imaging reflection T1. For the 20 s sweep, the source generated strong surface waves signal and, therefore, it was hence excluded. The 16 s sweep was also excluded due to the signal attenuation at longer offsets and at depth (>0.75 s). The choice of the 17 s sweep length was made after considering the large number of planned shot points (more than 950 shot points, ~3000 sweeps). However, an 18 s

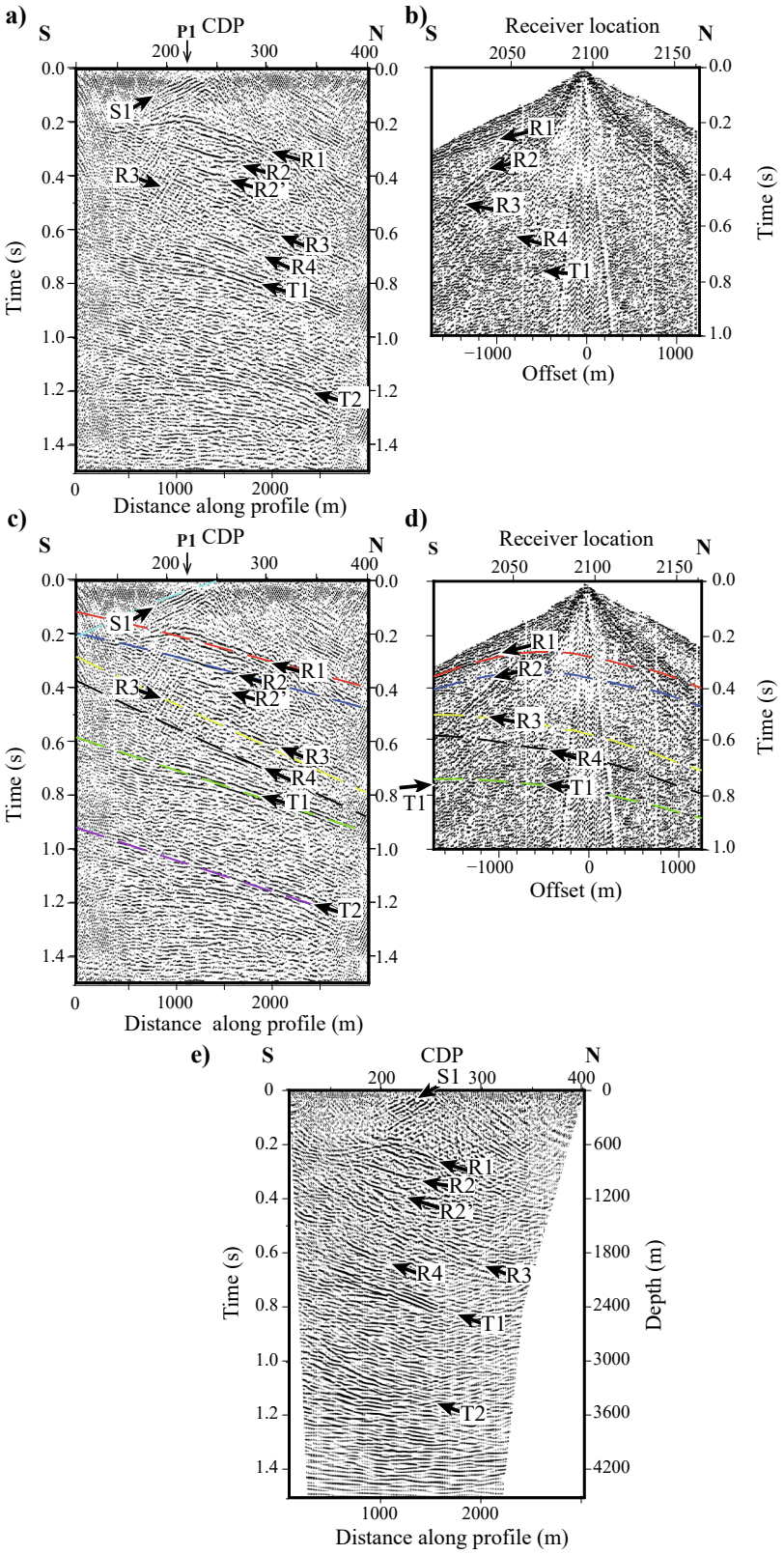

Fig. 7. (a) Unmigrated stacked section and (b) example of a processed shot gather along P2. Traveltimes calculated using the 3D reflection traveltime modelling on (c) the unmigrated stacked section and (d) the shot gather. The modelled traveltimes for reflections S1, R1-R4 and T1 match the observed traveltimes both in the shot gather and the stacked section. (e) Migrated and time-to-depth converted section of P2.

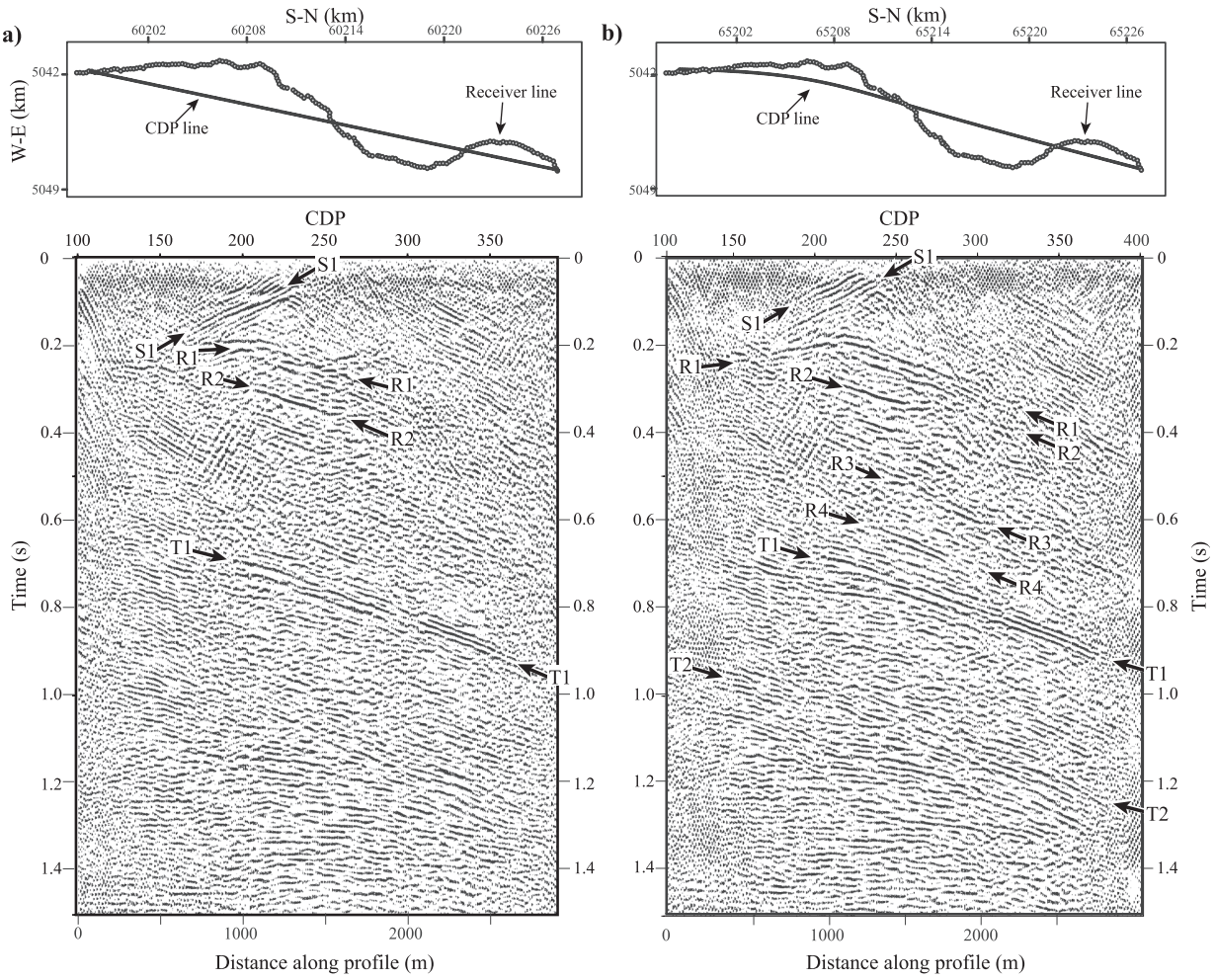

Fig. 8. Unmigrated stacked section of P2 showing sub-horizontal to more steeply dipping reflections obtained using (a) a straight or (b) a slalom CDP line. A slalom CDP line was chosen in this study because the continuity and sharpness of the reflections are better compared to the straight CDP line.

sweep length would have also produced high quality data.

4. Data processing

Seismic profiles were designed to cover all of the Zinkgruvan mining area, particularly north of the mineshaft, where the mineral potential is thought to be higher. All forest tracks and trails were used in the survey, particularly if they could host source positions. Sometimes this resulted in significant amounts of noise due to their proximity to the power lines and/or roads. Reflections in raw shot gathers were sometimes difficult to identify due to, for example, power line induced electromagnetic noise. An example is shown in Fig. 5a–c. A 50 Hz noise is evident in many shot gathers, particularly along P8 (Fig. 5c). However, raw shot gathers along P1 (Fig. 5a) show greater potential for high-resolution imaging. Several reflections within the shallow subsurface plus a deep reflection at 700–800 ms are observed. Shot gathers along P2 (Fig. 5b) present a low signal-to-noise ratio (S/N) for the first 66 receiver positions due to the proximity to the power line and a much better resolution at the northern part of the profile. Data processing was particularly challenged by the low S/N along these parts of P2 and P8.

The processing flow (Table 2) started with cross-correlating the raw data with the theoretical sweep. The geometry of the shots and receivers including CMP or CDP (common mid/depth point) was added to the seismic traces. Refraction and reflection residual statics, notch filter and normal moveout (NMO) corrections had the greatest influence on the processed stacked sections. Good refraction statics were key in the processing workflow given the varying topography and likely different depth to bedrock along the profiles. Refraction statics required accurate picking of the first breaks. Accordingly, first breaks were picked carefully by examining and tuning all the automatically and manually generated picks. The importance of the refraction static correction was evident after observing the improved continuity of the first arrivals and the enhanced coherency of later reflections. After applying a notch filter, designed to remove the 50 Hz harmonic noise, some improvements were made in the seismic records of P2 and P8 (Fig. 5d–f). To further enhance the S/N, a median filter using a velocity of 2500 m/s was applied to attenuate the source-generated shear waves. Then a broad band-pass filter was applied to the data keeping frequencies between 30 and 120 Hz. This partly removed some of the surface-waves but a strong portion remained. To make sure surface-waves would not stack in, a spectral equalization filter was applied between 40 and 100 Hz to reduce their energy signal in the shot gathers. Later a top-mute function, using the first breaks, was used to make sure first arrivals would not leak as steep events in the final stacked section. Fig. 5 shows shot gathers before and after the various processing steps (i.e. refraction statics, notch filter, median filter and trace editing), demonstrating that the pre-stack processing workflow clearly enhanced the reflections in all of the three profiles. The processing workflow did not intend to preserve low frequencies generated by the source in this current work, as surface-waves remained dominant and difficult to attenuate without filtering frequencies below 40 Hz. Future research could take an approach and develop solutions to remove surface-waves without any frequency-type

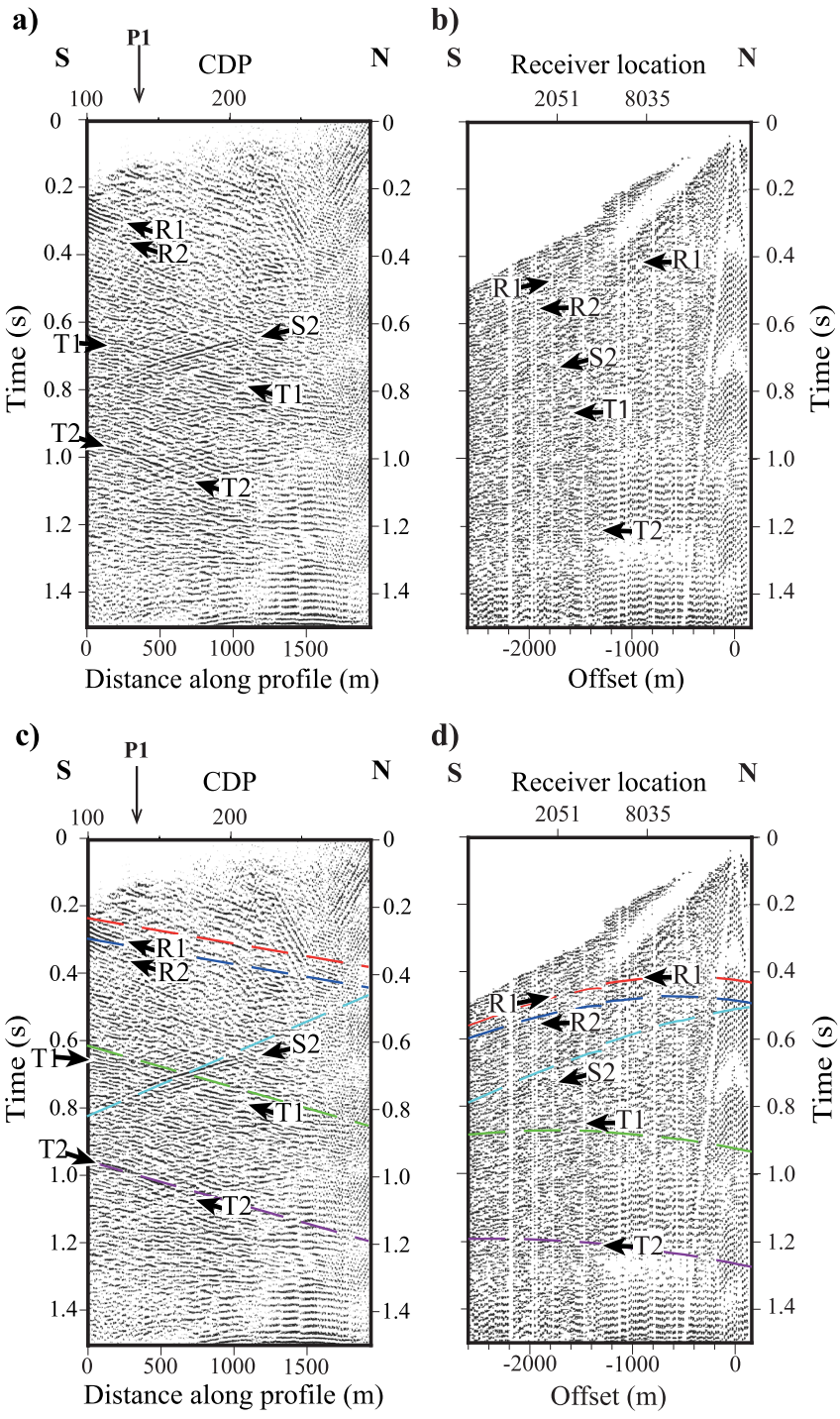

Fig. 9. (a) Unmigrated stacked section and (b) example of a processed shot gather along P8. Traveltimes calculated using the 3D reflection traveltime modelling on (c) the unmigrated stacked section and (d) the shot gathers. Not the extreme noisy character of the data along P8. The unmigrated stacked section, however, shows a set of reflections (e.g., R1-R2, T1-T2 and S2). Note that reflection labels are identical throughout the paper as they represent the same geological features, which are modelled in all the three seismic profiles (P1, P2 and P8). This means that if modelled traveltimes match the reflections in P8, they also do match them along P1 and P2.

filtering procedure (e.g., Balestrini et al., 2020).

The quality of the unmigrated stacked sections was related to the velocity used for NMO corrections. The dipping reflections stacked coherently with high NMO velocities, while lower NMO velocities were used to stack sub-horizontal reflections. Generally, the application of dip moveout (DMO) allows crossing steeply and gently dipping reflections to stack simultaneously. However, for this dataset, we were unable to obtain a clear image of the dipping reflections with the application of DMO. This may be due to (1) reflections might come from out-of-the-plane features, (2) irregular shot spacing, and (3) the crookedness of the profiles, which makes the offset distribution irregular, a prerequisite for a successful DMO-based imaging (Deregowski, 1986; Juhlin et al., 2010).

In theory, if the reflections are originated within-the-plane of the profiles, the migration (when correct velocity is used) process should locate them at their correct spatial position, and with their corresponding true dips. We used a finite-difference algorithm for the migration that was followed by a depth conversion using a constant velocity of 6000 m/s, which is an average velocity extracted from sonic logs (shown later) in the area. Fig. 6a and 7a present P1 and P2 unmigrated stacked sections, respectively, and Fig. 6e and 7e the same sections after the migration. Along P1 (Fig. 6e), reflections appear to be straight (e.g., R1 and R2) whereas along P2 they present a change of dip, having a curved shape. This could be related to the crookedness of the

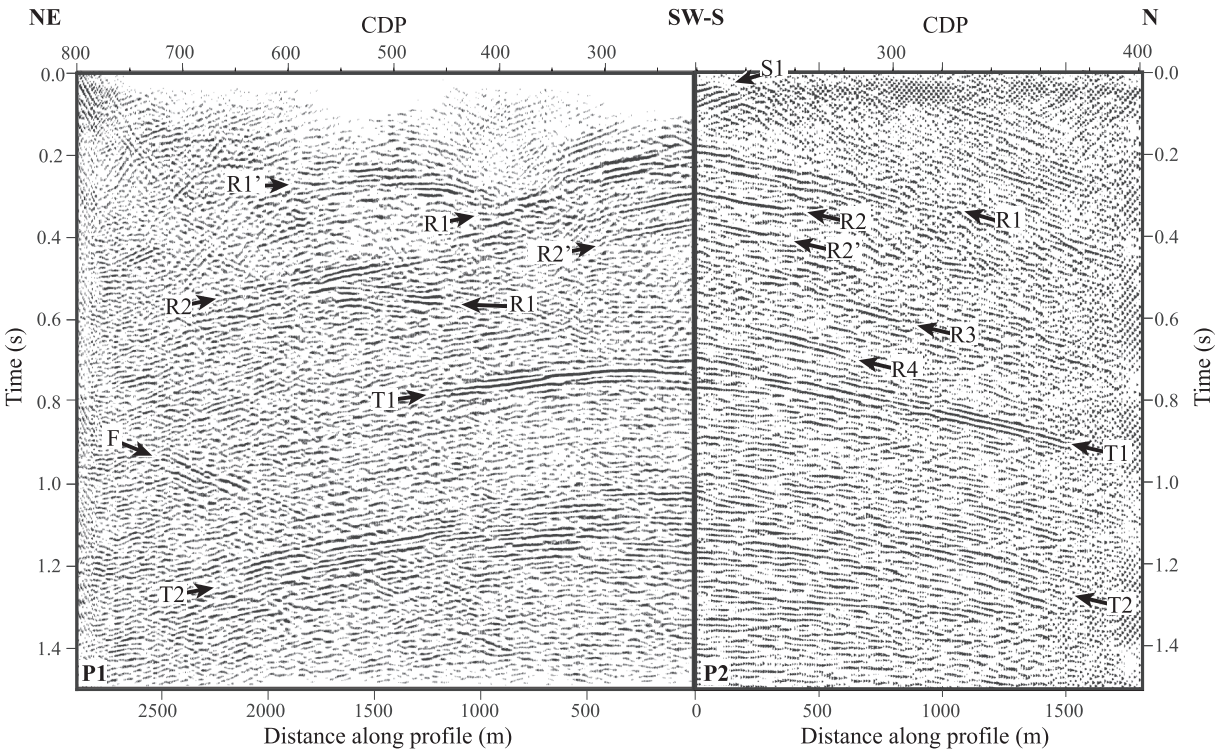

Fig. 10. Unmigrated stacked section of the eastern part of P1 and the northern part of P2 merged at their intersection point. Different reflections (e.g., R1-R2, T1-T2) traveltimes match better in the unmigrated section showing how they have been consistently imaged in these profiles. This figure also illustrate that all these reflections have an apparent dip in their corresponding profile and that the true dip is to the NE.

Table 3
Main reflectors and their geometry as determined from the 3D reflection traveltime modelling.

Reflector	Strike[a]	Dip	Distance (m)[b]	Depth (m)[c]	Rank[d]
S1	40	80	2000		1
R1	320	20		320	1
R2	320	20		620	1
R3	270	30		866	1
R4	270	30		1155	2
T1	275	20		1965	3
T2	275	20		2965	3
S2	45	25		1930	2

[a] Considering north as reference.
[b] Distance refers to longitudinal from an arbitrary model origin (Reference point in Fig. 11) to the closest point on the reflector's surface trace.
[c] Depth refers to vertical depth below the surface at the origin of the model.
[d] Rank indicates confidence in the identification; 1 = definite and validated from VSP data, 2 = probable and 3 = highly speculative.

survey line and the slalom CDP line defined for the processing. To carefully study the effect of a straight or slalom CDP line choice, we tested these scenarios along P2 (Fig. 8). The slalom CDP line (Fig. 8b) fails to identify the shallowest reflections (S1), which are sharply visible in the straight CDP line stacked section (Fig. 8a). Obviously, some of the reflections change their dip (e.g., T1) and character. Nevertheless, the slalom CDP line appears to image more reflections (e.g., R3 and R4), and more continuous (e.g., R1 and T2). Slalom CDP geometry was therefore used for the data along P1 and P2, while for P8 a straight S-N trending CDP line was used (Fig. 9). Because P8 was defined as a straight NS line, a straight CDP line was an obvious choice.

5. 3D reflection traveltime modelling and borehole data

Due to the complex geology in the Zinkgruvan mining area, one can assume that some of the observed reflections on the profiles may come from out-of-the-plane. Even if they are not, due to the crookedness of the lines, it is impossible to capture their true geometry using only a set of 2D profiles. 2D migration process will only migrate properly those reflections that lay completely within-the-plane of the profiles and will not be accurate for out-of-the-plane reflections (Herron, 2016; Malehmir et al., 2017a; Herron and Smith, 2019). Moreover, along P8 (Fig. 9a), the main reflections occur at the edges of the stacked section with inward dips and therefore they will migrate outside of the section. An example is reflection F that even though it is observed on the shot gathers and stack along P1 (Fig. 6a–d), after the migration process, this reflection migrates outside of the section (Fig. 6e), because it does not continue under the migrated section and rather a feature imaged beyond the horizontal length of the section. This is an advantage of post-stack imaging algorithms allowing such a feature to be seen and if necessary kept by padding the data. Once noted, obviously pre-stack imaging algorithm can also use the same approach.

When comparing seismic data from crossing profiles, unmigrated stacked sections are the best, as reflections should match in time. However, this would not be the case when data are migrated, even if pre-stack time or depth migration is used (Herron and Smith, 2019). As an example, reflection T1 is observed at approximately 800 ms on the NW side of P1 in the unmigrated stacked section (Fig. 6a), and at similar traveltimes in P2 (200 CDPs; Fig. 7a). This is not the case when the migrated sections are compared, as both sections do not feature a true dip of the reflection (Fig. 10). Accordingly, and due to the short offsets in P8, we will only use the unmigrated section for this profile.

In order to extract information on the 3D orientation of the most prominent observed reflections, both on the shot gathers and unmigrated stacked sections, 3D reflection traveltime modelling was carried out using the true acquisition geometry of the profiles and the CDP lines. A planar surface with specific dip, strike and distance from the profile was assumed for every reflector during the modelling. Then we calculate the traveltimes to this interface using a constant velocity of 6000 m/s for

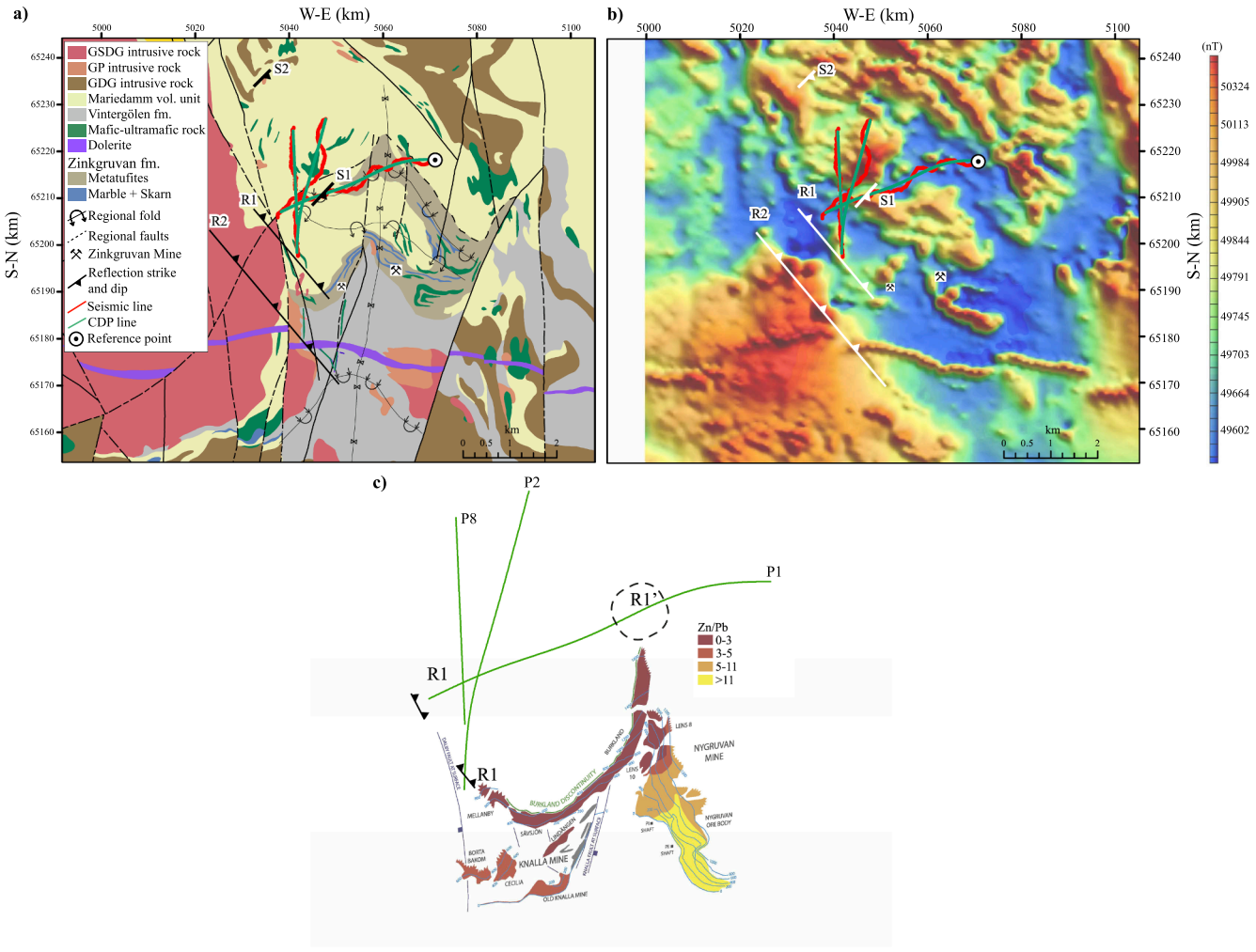

Fig. 11. Surface projection of the 3D traveltime modelled reflectors onto (a) the geological map and (b) the total-field aeromagnetic map of the Zinkgruvan mining area. Most of the modelled reflections correlated well with the magnetic lineaments representing various lithological boundaries. The thick circle at the eastern end of P1 marks the point to which the distances are referred to in Table 3. (c) Overview of the R1 and R1′ reflections with respect to the main Zinkgruvan Formation defined by Jansson et al. (2017). The Geological Survey of Sweden (SGU) has provided aeromagnetic data. The geological map is modified from SGU database and Jansson et al. (2017) interpretations.

the media, as this is consistent with the velocities observed in the first arrivals, NMO and sonic logs. The geometry of the planar surface (i.e., dip and strike) is changed until the calculated 3D reflection traveltimes fit the observed traveltimes on both the shot gather and the stacked section (Ayarza et al., 2000). Fig. 6c,d, 7c,d and 9c,d show examples of fitting traveltimes, calculated by following Ayarza et al. (2000) method, for the most prominent reflections (S1, R1, R2, T1 and T2) on both shot gathers and unmigrated stacked sections for P1, P2 and P8, respectively. The final results (e.g., strike and dip of the potential reflector) of the reflection traveltime modelling are summarised in Table 3. The 3D traveltime modelling work does not generate synthetic traces although this is possible by 1D-convolution. The fact that the same modelled reflectors match the traveltimes of observed reflections in both shot gathers and unmigrated stacked sections in all the three profiles provides a certain level of confidence about the uniqueness and correct geometry of the modelled surfaces. This also implies that the velocity of 6000 m/s used for migration and time-to-depth conversion is a good choice and not far from reality.

From the traveltime modelling study on the shot gathers and on the unmigrated stacked sections, we determine that most of the reflections (e.g., R1–R4, and T1–T2) originate from the southwest of the profiles, strike ~ E-W to NW-SE, and dip between 20° and 30° to the northeast (Figs. 6–10 and Table 3). On the other hand, S1 and S2 come from features striking NE-SW and dipping to the SE. Reflector S1 appears to be located between P1 and P2, as shown in Fig. 10. The reflection traveltime modelling also supports this, as only the shot gathers located on the western end of P1 are able to image this reflector. Similarly, only a few first shot gathers along the first 140 CDPs (1400 m) of P2 show S1. The surface projections of the deepest reflections (i.e., T1 and T2) seem to correlate with clear magnetic lineaments from mafic to ultramafic sill-like intrusions or diorite dykes, as observed in the geological and magnetic field map (Fig. 11). Considering that the gentle dip of T1 and T2 reflections (Table 3) and that they do not seem to crosscut shallower reflections (as shown in Figs. 8–10), we associate their origin with lava-flows (mafic–ultramafic volcanic intrusions) within the stratigraphy, as they are abundantly seen in the geological map concordant with the overall stratigraphy. Reflections R1 and R2 correlate with the main Zinkgruvan Formation defined by Jansson et al. (2017), where R1 crossing P1 and P2 at the south-western and R1′ is visible in the middle of P1 (Fig. 11).

To further constrain the interpretation of the nature and origin of the reflections, a limited number of downhole logging data, provided by Zinkgruvan Mining AB, were used. As P8 reflections migrate outside of the stacked section, we decided to focus on downhole logging data that cross profiles P1 and P2. Density and sonic logs (BH3991, BH2710 and BH2726), as well as the acoustic impedance calculated from these, were

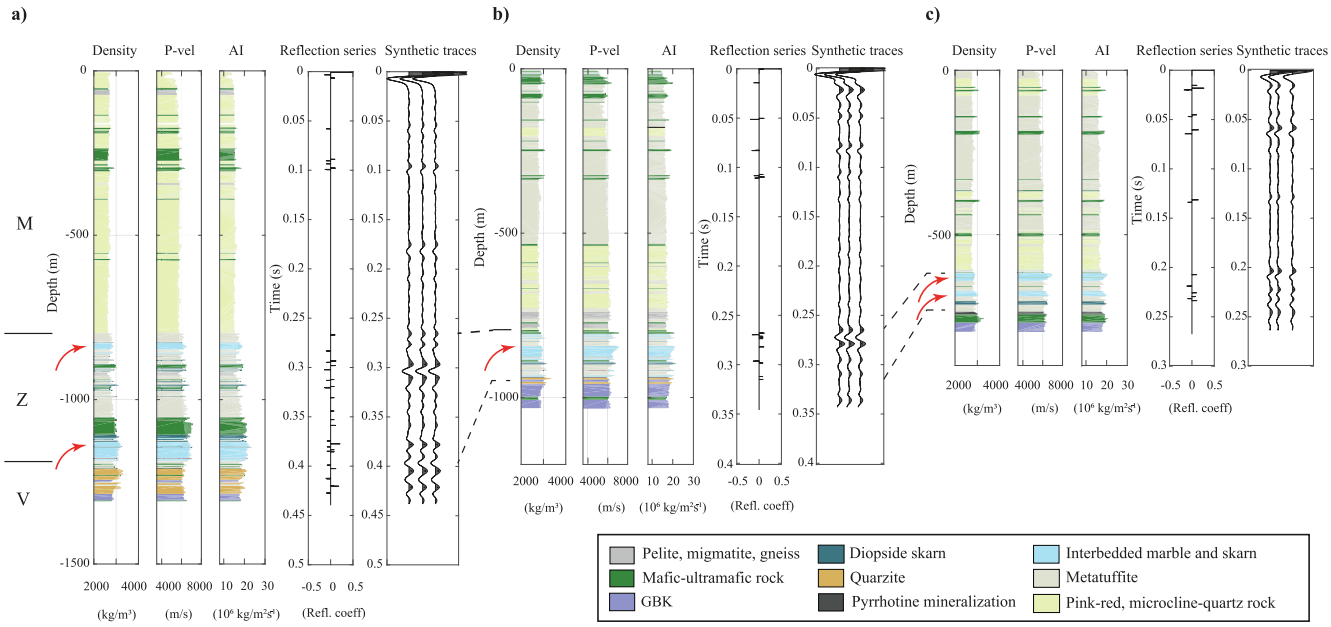

Fig. 12. Example of downhole logging data from three boreholes (from west to east; see Fig. 1) (a) BH3991, (b) BH2726, and (c) BH2710 in the Zinkgruvan mining area. Reflection time series were calculated from the acoustic impedance, and synthetic traces were generated by convolving the reflection time series with a 60 Hz Ricker wavelet. The different formations (Fig. 2) have been correlated using the dashed lines between the boreholes. As illustrated here, the Zinkgruvan Formation should be reflective both on its hanging- and footwalls due to the sharp acoustic impedance contract changes. Zinkgruvan is the main host of the mineralization in the study area. V: Vintergölen Formation; Z: Zinkgruvan Formation; M: Mariedamm volcanic unit.

considered. From the acoustic impedances, the reflection time series were calculated, and then synthetic traces were generated by convolving the reflection series with a 60 Hz Ricker wavelet (Fig. 12). These boreholes cross the Zinkgruvan Formation and part of the Mariedamm volcanic unit. Fig. 12 displays a complete set of the downhole logging measurements from the three boreholes. As stated before, average velocities down to 1200 m depth are around 6000 m/s. The standout feature in these logs is, however, the increase in the acoustic impedance at the boundary between Mariedamm and Zinkgruvan thus making the boundary a potential source of reflectivity. Also, the Zinkgruvan Formation shows alternating lithologies that result in an increase on the acoustic impedance contrast and, therefore, a strong seismic response (Fig. 12). This is due to interbedded layers of marble and skarn, where the zinc mineralization is present (Jansson et al., 2017, 2018; Fig. 2). The acoustic impedance decreases sharply at the boundary between the Zinkgruvan and Vintergölen formations making this boundary also an important source of reflectivity. Amphibolite intrusions also present high-acoustic impedance, and strong seismic response, but those are often localised, and can be found along the entire Zinkgruvan Formation. If amphibolites are thick enough, they can potentially be reflective and complicate the interpretation of the seismic data (Fig. 12). Note that the stratigraphic sequence shown by the boreholes is inverted, implying that they lie on the inverted limb of a fold.

6. Results, interpretation and discussion

The seismic sections show a series of gently to moderately dipping (e.g., S1) and sometimes sub-horizontal (e.g., T1 and T2) reflections. Only reflections R1-R1′ shows both, a sub-horizontal and a steeply dipping character at different CDP ranges along P1 (Fig. 6). We interpret some of these reflections based on the available geological observations, magnetic data and the visualization of the seismic sections as pseudo 3D (Figs. 11–14). The results of 3D reflection traveltime modelling will also be used to constrain the interpretations.

Fig. 13 shows the correlation between the downhole logs and the migrated P1 and P2 sections. The projection of the borehole logs onto the seismic sections shows that reflections S1 and R1–R3 correlate well with regions where a sharp change in velocity-density associated with lithological changes occur. Boreholes BH2710 and BH2726 plunge 16.3° and 13.5° towards the southeast, respectively (Fig. 1). BH2726 crosses both P1 and P2; at 150 m depth intersects P2, while at 350 m depth intersects P1. This is better depicted using 3D visualization of the data as shown in Fig. 14b. According to BH2726 log data, two high acoustic impedance contrast zones at 50 and 100 m depths (Fig. 12) correlate with reflection S1 on the migrated section of P2 (Fig. 13d). Reflection S1 intersects both P1 and P2 (Fig. 10), showing a prominent dip towards the southeast (Table 3). We speculate that reflection S1 originates from a series of mafic (high velocity-density) intrusions. The reflection traveltime modelling suggests that this reflection should also be observed on the first 50 CDPs in P8, (between CDPs 100 and 150) at around 150 ms. Unfortunately, P8 does not show this reflection due to the lack of near-offset data (Fig. 9).

Reflections R1 and R2 also correlate reasonably well with regions of significant impedance contrasts identified at the borehole logs (Fig. 13). The set of reflections identified as R1 are related to the Zinkgruvan Formation. This band of reflectivity clearly starts to be observed at around 600 m, the depth at which the boundary between the Mariedamm volcanic unit and Zinkgruvan Formation is found in BH2710 (Figs. 12 and 13c). Reflection R1′ (Fig. 13a, 14a-b) at 900 and 1650 m depths has an out-of-the-plane nature and is associated with the top of the Zinkgruvan Formation as it approaches P1 from the south and turns as R1 into P1 from its eastern side. This means that R1′ and R1 have identical origin, but they are seen at different offsets in P1 due to the geometry of this boundary and that of the crooked seismic survey line. The fact that R1′ features such a high amplitude implies a strong impedance contrast such as the Zinkgruvan Formation hosting the stratiform Zn-Pb-Ag-(Cu) mineralization (Jansson et al., 2017, 2018). In Fig. 13a, R1 reflection features a depression at around 900 m depth, between CDPs 300 and 500. The current model of the mineralization (not presented here) shows a similar pattern at this region and depth indicating that the Zinkgruvan Formation is affected by folding. The seismic data clearly depict this depression and illustrate its power in resolving such small features (Fig. 13a) when sufficient impedance contrasts exist.

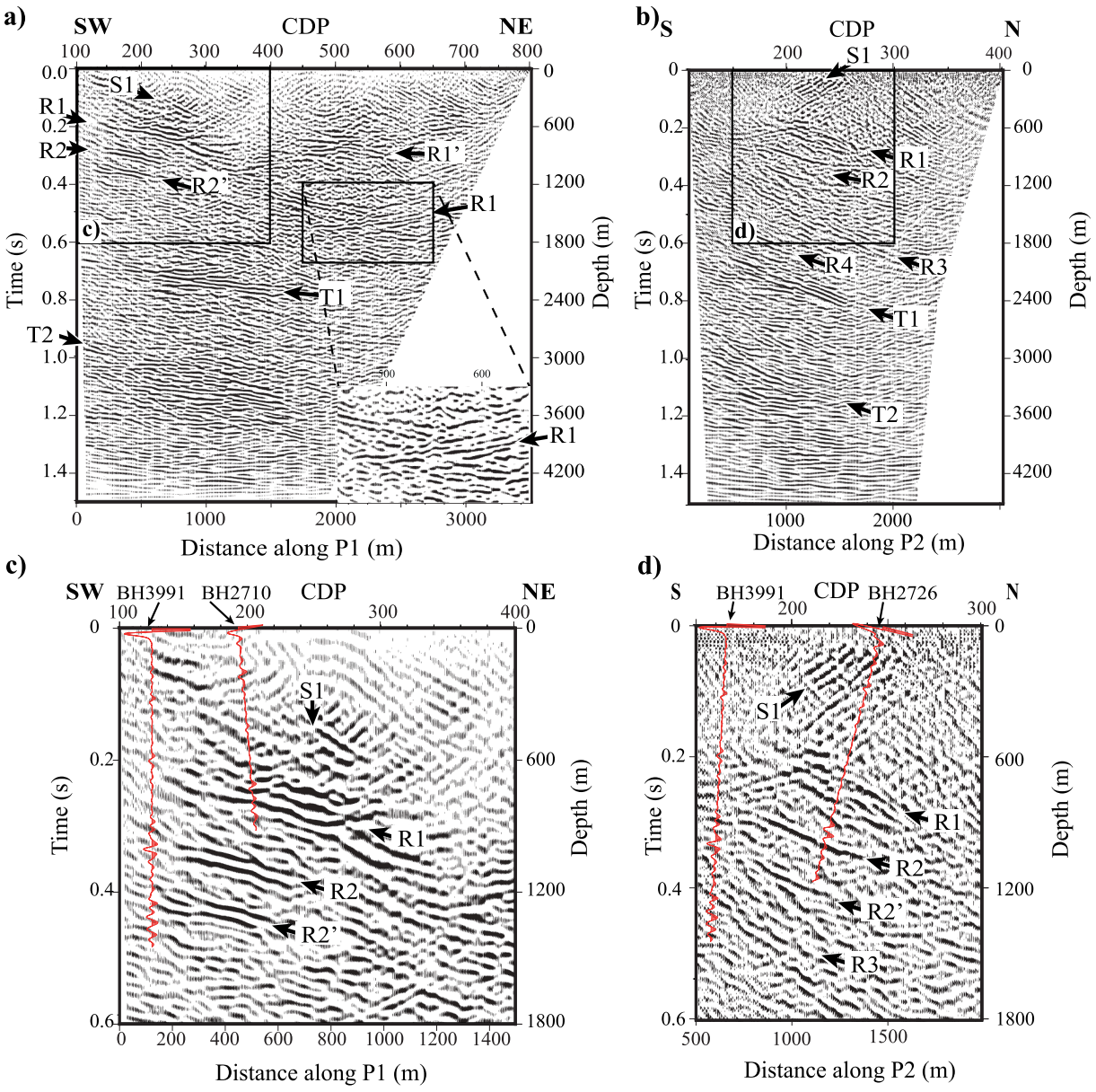

Fig. 13. (a-b) Migrated stacked sections of P1 and P2 with projected (c-d) synthetic traces from BH2710, BH2726 and BH3991 showing how reflections R1 and R2 correlate with the Zinkgruvan Formation and reflection R2 with the top of the Vintergölen Formation. Black arrows mark different reflections detailed in the text. Note the depicted depression of R1 reflection between 450 and 650 CDPs.

Borehole BH3991, which is located between P1 and P2 (Figs. 1 and 14c), intersects P1 seismic section at 800 m depth. This suggests that reflection R2 is associated with the interbedded marble and skarn units on top of the Zinkgruvan Formation, while the R2′ can be related to the boundary between the marble and skarn units of the Zinkgruvan Formation and the GBK rocks of the Vintergölen Formation (Figs. 2, 12 and 13c). If we project BH3991 onto P2 (Fig. 13d), the reflection R3 correlates with the intercalation of GBK and quartzites within the Vintergölen Formation. In fact, this unit is probably the reason for reflections R3 and R4. Reflections R2 and R2′ are associated with the top and bottom of the Zinkgruvan Formation. R1 reflection also corresponds to the boundary between the Zinkgruvan Formation and the Mariedamm volcanic unit, but as pointed out earlier, R1 migrates out of the section and from the reflection traveltime modelling results it also as an out-of-the-plane character (Figs. 12, 13a and 14). This means R1 has an oblique strike to the orientation of both P1 and P2. These results suggest that the Zinkgruvan Formation together with the 'Emme Group' plunge towards the northeast, agreeing also with the previous studies of Kumpulainen et al. (1996) and Jansson et al. (2017), Jansson et al. (2018). This interpretation implies that the mineralization also dips locally towards the northeast within the study block, making it a highly prospective area. NS folding affecting the area will surely change its dip towards the east.

We argue based on the available borehole data and the strong amplitude nature of R1′ that it is located south of P1 and is likely from the mineralization sitting within the crest of a folded smaller antiform (of Zinkgruvan Formation) that plunges to the north (Fig. 1). As mentioned earlier, the downhole data show that the Zinkgruvan Formation dips towards the NE at BH3991 and BH2726 (Fig. 12a-b), while BH2710 (Fig. 12c) suggests that the formation presents a dip towards the NW. Although from the seismic data we observed that the Zinkgruvan Formation presents a dip towards the NE, as BH3991 and BH2726 indicate, the variation of the dip, observed from BH2710, where the Zinkgruvan Formation is found at 600 m, could be related to a change of the geological dip due to the NS folding that affects the Zinkgruvan mining area (Figs. 1, 11 and 12).

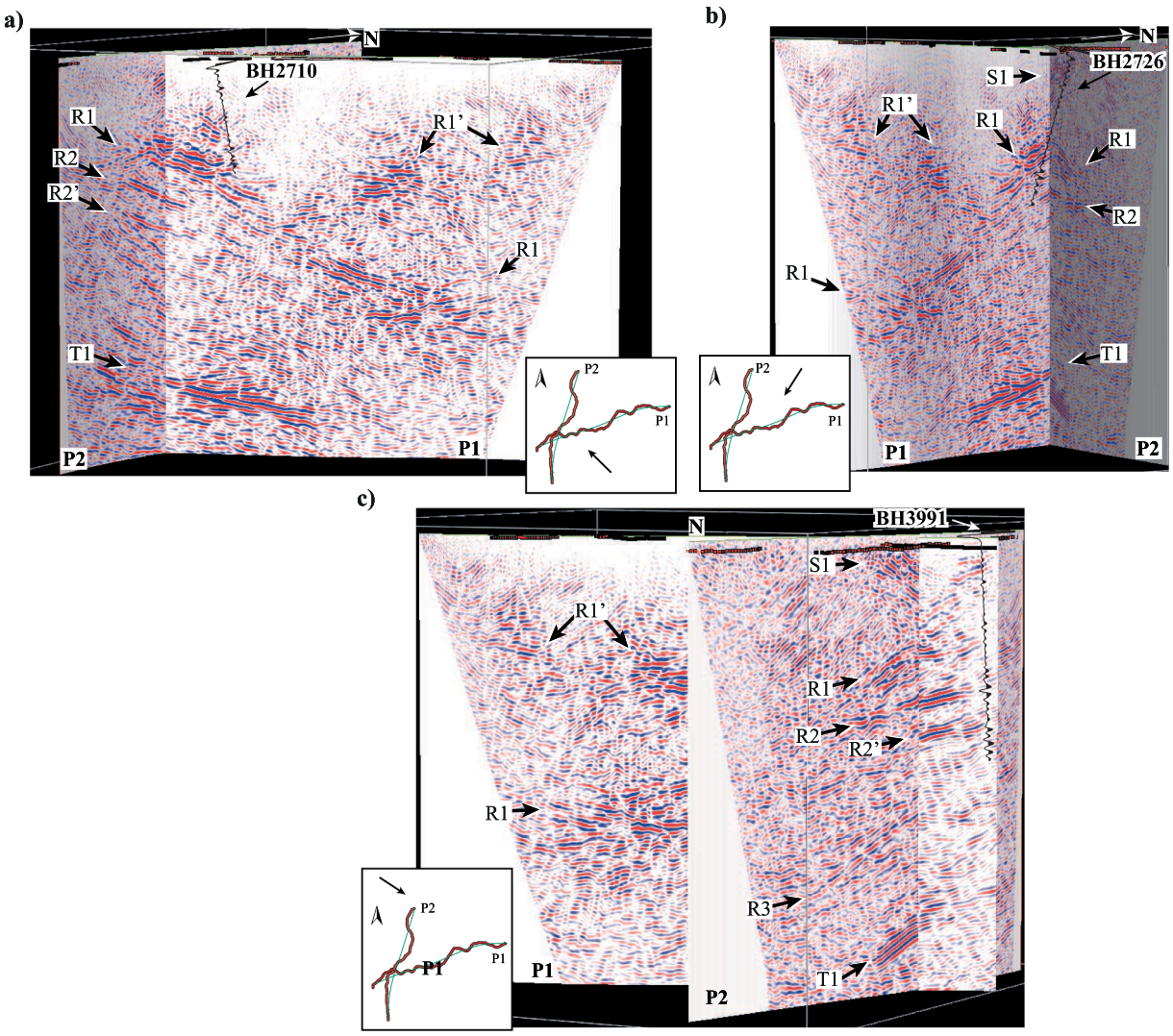

Fig. 14. Various 3D views of the migrated stacked sections of P1 and P2 showing how different reflections correlate in different boreholes (a) BH2710, (b) BH2726 and (c) BH3991. Note BH2726 intersects both profiles. The black arrows in the encapsulated maps show the perspective view of the 3D models.

7. Application of high-resolution seismics in noisy hard rock settings

7.1. Relevance to deep mineral exploration

One of the key results of this study is the demonstration that seismic methods can delineate key lithological boundaries that potentially host base-metal deposits. Although the area is strongly deformed by two different stages of folding and several fault systems, the Zinkgruvan Formation that hosts the stratiform Zn-Pb-Ag-(Cu) mineralization can be imaged on the shot gathers and stacked sections. Fig. 14 shows 3D views of the migrated P1 and P2 sections that suggest that the bottom of the Zinkgruvan Formation, where the base-metal deposits are located, can be imaged by seismic data. This is encouraging and should open possibilities to conduct additional seismic surveys in the Bergslagen district for base-metal exploration in general. In this work, the seismic methods have been proven to be effective in a tectonic setting such as Bergslagen, because they have clearly mapped important mineral-bearing units and can aid deep exploration in the district.

7.2. Seismic imaging with different receivers

The three seismic profiles presented here employed receiver spreads with different parameters (geophone natural frequency, sampling interval and receiver spacing; Table 1). However, they all managed to image several deep reflections (e.g., T1, T2 and S2), some of them with an out-of-the-plane origin (Fig. 9). Nevertheless, a dominant feature of the seismic data, particularly along P8 and the southern portion of P2, is the high level of contamination with 50Hz periodic noise from the power lines. While it is still possible to identify and image the most energetic reflections such as T1, weaker reflections might have suffered from severe notch filtering (Fig. 5a,b). When the quality of the P1 and P2 data is compared with that of P8, this fact (noisy nature of P8) is quite notable. Therefore, we suggest that future surveys should benefit from digital sensors. Brodic et al. (2015) and Brodic et al. (2017) illustrated that MEMS (micro-electro-mechanical system) sensors are superior to geophones in such cases, as they do not appear to pick up electric or electromagnetic noise from power lines in urban and tunnel projects. This can particularly be helpful in this part of the study area along the power line.

7.3. Future studies

While this study provides a first-hand picture of the seismic data for deep exploration in a noisy mining environment, more seismic profiles are available, and their processing could provide additional constraints

on the nature of different structures observed in this study. This will be done soon, and the results integrated with those of the application of 3D imaging tools (e.g., PSDM). Given the sparse acquisition lines and shots, we, however, anticipate severe acquisition footprints (e.g., Cheraghi et al., 2012; Malehmir et al., 2021) when 3D imaging algorithms are used, an issue that will require careful dedication, which is beyond the scope of this work.

8. Conclusions

Ten reflection seismic profiles have been acquired in the Zinkgruvan geological complex and noisy mining area. Three seismic profiles have been processed to image the main subsurface geological structures. These profiles show various reflections from high quality, rich in reflectivity, to noisy due to power lines and mining activities in the underground mine. Nonetheless, clear reflections are observed in the shot gathers thanks to the careful setup of the lines and source parameters used for the survey. 3D reflection traveltime modelling was combined with borehole logs and geological and aeromagnetic maps, to produce a joint subsurface interpretation of the study area. This helped to capture the pseudo-3D orientation of the main reflections, understand their possible out-of-the-plane nature and associate them with key geological markers. In particular, two sets of reflections are interpreted to originate from the Zinkgruvan Formation where mineralization is hosted. This Formation shows various character and geometry in the profiles with even a possible repetition due to its complex 3D geometry footprint in the 2D sections. A general northeast dip is observed for these reflections suggesting that deep targeting and exploration can focus in this direction. Other reflections are interpreted to be from intrusions, particularly the deeper ones as they can well be correlated with an NE-SW striking magnetic lineament observed south of the study area.

This study shows how complementary high-resolution reflection seismic data can be instrumental in helping to constrain large-scale geological features in a mining environment. Although we used different recorders with varying geophone natural frequency, strong reflections were imaged in these profiles regardless of their different seismic folds and lengths. Moreover, this study should open up new possibilities for using reflection seismic methods for exploration and geological mapping in the Bergslagen region, where the geology is believed to be highly complex and affected by various tectonic stages and metamorphism.

Declaration of Competing Interest

The authors declare that they have no known competing financial interests or personal relationships that could have appeared to influence the work reported in this paper.

Acknowledgments

EIT-RawMaterials is gratefully thanked for funding this up-scaling project 17024. We thank many colleagues from the Institute of Earth Sciences Jaume Almera (CSIC, Barcelona), Technische Universität Bergakademie Freiberg and Uppsala University for their support during the field experiment, in particular, Bojan Brodic and Nanna Sørensen. We also thank DMT, SGU, Zinkgruvan Mining AB and Lundin Mining for their collaboration and support. We are grateful to the Geophysical Instrument Pool Potsdam (GIPP) for providing geophones and wireless recorders. GLOBE Claritas™ under license from the Institute of Geological and Nuclear Sciences Limited, Lower Hutt, New Zealand was used to process the seismic data. GOCAD Consortium and Paradigm are thanked for providing an academic license of GOCAD for 3D visualization and interpretation of the data. GMT from P. Wessel and W.H.F Smith was used to prepare some of the figures. The authors acknowledge the usage of the Vibroseis truck of Technische Universität Bergakademie Freiberg, operated by the Institute of Geophysics and Geoinformatics and funded by the Deutsche Forschungsgemeinschaft (DFG) under grant no. INST 267/127-1 FUGG. We thank the editor and two anonymous reviewers for their constructive and critical comments that helped to improve an earlier version of this article.

References

Adam, E., Milkereit, B., Mareschal, M., Barnes, A.E., Hubert, C., Salisbury, M., 1992. The application of reflection seismology to the investigation of the geometry of near-surface units and faults in the Blake River Group, Abitibi Belt, Quebec. Can. J. Earth Sci. 29, 2038–2045. https://doi.org/10.1139/e92-160.

Alaei, B., Torabi, A., 2017. Seismic imaging of fault damaged zone and its scaling relation with displacement. Interpretations 5, SP83–SP93. https://doi.org/10.1190/INT-2016-0230.1.

Allen, R.L., Lundström, I., Ripa, M., Simeonov, A., Christofferson, H., 1996. Facies analysis of a 1.9 Ga, continental margin, back-arc, felsic caldera province with diverse Zn-Pb-Ag-(Cu-Au) sulphide and Fe oxide deposits, Bergslagen Region. Sweden. Econ. Geol. 91, 979–1008.

Allen, R.L., Bull, S., Ripa, M., Jonsson, R., 2003. Regional Stratigraphy, Basin Evolution, and the Setting of Stratabound Zn-Pb-Cu-Ag-Au Deposits in the Bergslagen, Sweden, SGU-FoU project 03-1203/99, Geological Survey of Sweden and Boliden Mineral AB, p. 80.

Ayarza, P., Juhlin, C., Brown, D., Beckholmen, M., Kimbell, G., Peching, R., Pevzner, I., Pevzner, R., Ayala, C., Bliznetsov, M., Glushkov, A., Rybalka, A., 2000. Integrated geological and geophysical studies in the SG4 borehole area, Tagil Volcanic Arc, Middle Urals: location of seismic reflectors and source of the reflectivity. J. Geophys. Res. 105, 21333–21352. https://doi.org/10.1029/2000JB900137.

Ahmadi, O., Juhlin, C., Malehmir, A., Munk, M., 2013. High-resolution 2D seismic imaging and forward modelling of a polymetallic sulphide deposit at Garpenberg, central Sweden. Geophysics 78, B339–B350.

Balestrini, F., Draganov, D., Malehmir, A., Marsden, P., Ghose, R., 2020. Improved target illumination at Ludvika mines of Sweden through seismic-interferometric noise reduction. Geophys. Prospect. 68, 200–213.

Beunk, F.F., Kuipers, G., 2012. The Bergslagen ore province, Sweden: Review and update of an accreted orocline, 1.9-1.8 Ga BP. Precambr. Res. 216–219, 95–119. https://doi.org/10.1016/j.precamres.2012.05.007.

Brodic, B., Malehmir, A., Juhlin, C., Dynesius, L., Bastani, M., Palm, H., 2015. Multicomponent broadband digital-based seismic landstreamer for near-surface applications. J. Appl. Geophys. 123, 227–241. https://doi.org/10.1016/j.jappgeo.2015.10.009.

Brodic, B., Malehmir, A., Bastani, M., Mehta, S., Juhlin, C., Lundberg, E., Wang, S., 2017. Multi-component digital-based seismic landstreamer and boat-towed radio-magnetotelluric acquisition systems for improved subsurface characterization in the urban environment. First Break 35, 41–47.

Buntin, S., Malehmir, A., Koyi, H., Högdahl, K., Malinowski, M., Larsson, S., Thybo, H., Juhlin, C., Korja, A., Górszczyk, A., 2019. Emplacement and 3D geometry of crustal-scale saurcer-shaped intrusions in the Fennoscandian Shield. Sci. Rep. 9, 1–11. https://doi.org/10.1038/s41598-019-46837-x.

Buske, S., Bellefleur, G., Malehmir, A., 2015. Introduction to Special Issue on "Hard Rock Seismic Imaging". Geophysical Prospecting, 65, 751–753. doi:10.111/1365-2478.12257.

Cheraghi, S., Malehmir, A., Bellefleur, G., 2012. 3D imaging challenges in steeply dipping mining structures: New lights on acquisition geometry and processing from the Brunswick no. 6 seismic data, Canada. Geophysics 77, WC109–WC122. https://doi.org/10.1190/geo2011-0475.1.

Dehghannejad, M., Juhlin, C., Malehmir, A., Skyttä, P., Weihed, P., 2010. Reflection seismic imaging of the upper crust in the Kristineberg mining area, northern Sweden. J. Appl. Geophys. 71, 125–136. https://doi.org/10.1016/j.jappgeo.2010.06.002.

Deregowski, S.M., 1986. What is DMO? Fisrt Break 4, 7–24. https://doi.org/10.3997/1365-2397.1986014.

Donoso, G.A., Malehmir, A., Pacheco, N., Araujo, V., Penney, M., Carvalho, J., Spicer, B., Beach, S., 2019. Potential of legacy 2D seismic data for deep targeting and structural imaging at the Neves-Corvo massive sulphide-bearing deposit, Portugal. Geophys. Prospect. 68, 44–61. https://doi.org/10.1111/1365-2478.12861.

Eaton, D., Milkereit, B., Salisbury, M., 2003. Mature technologies adapted to new exploration targets, Foreword to hardrock seismic exploration. In Hardrock Seismic Exploration, 1–6. Society of Exploration Geophysics.

Gaál, G., Gorbatschev, R., 1987. An outline of the Precambrian evolution of the Batlic Shield. Precambrian Research, 35, 15–52.15-52.

Geijer, R., 1917. Falutraktens berggrund och malmfyndigheter. Sver. Geol. Unders C 275, 316.

Gupta, R.R., 1971. Seismic determination of geological discontinuities ahead of rapid excavation. Semi Annual report No. 6051: Bendix Research Laboratory, 40.

Herron, D., 2016. A simple procedure for handling misties on 2D migrated seismic lines. Interpretation 4, B17–B21. https://doi.org/10.1190/INT-2016-0012.1.

Herron, D., Smith, T., 2019. Practical aspects of working with 2D migrated seismic data. Interpretation 7, SG1–SG9. https://doi.org/10.1190/INT-2018-0189.1.

Hedström, P., Simeonov, A., Malmoström, L., 1989. The Zinkgruvan ore deposit, south-central Sweden: Proterozoic, proximal Zn-Pb-Ag deposit in distal volcanic facies. Econ. Geol. 84, 1235–1261.

Humphreys, D., 2018. The mining industry after the boom. Min. Econ. 32, 145–151. https://doi.org/10.1007/s13563-018-0155-x.

Jansson, N.F., Zetterqvist, A., Allen, R.L., Billström, K., Malmström, L., 2017. Genesis of the Zinkgruvan stratiform Zn-Pb-Ag deposit and associated delomite-hosted Cu ore,

Bergslagen, Sweden. Ore Geol. Rev. 82, 285–308. https://doi.org/10.1016/j.oregeorev.2016.12.004.
Jansson, N.F., Zetterqvist, A., Allen, R.L., Malmström, L., 2018. Geochemical vectors for stratiform Zn-Pb-Ag sulphide and associated dolomite-hosted Cu mineralization at Zinkgruvan, Bergslagen, Sweden. J. Geochem. Explor. 190, 207–228. https://doi.org/10.1016/j.gexplo.2018.03.015.
Juhlin, C., Lindgren, J., Collini, B., 1991. Interpretation of seismic reflection and borehole data from Precambrian rocks in the Dala Sandstone area, central Sweden. First Break 9, 24–36.
Juhlin, C., Dehghannejad, M., Lund, B., Malehmir, A., Pratt, A., 2010. Reflection seismic imaging of the end-glacial Pärvie Fault system, northern Sweden. J. Appl. Geophys. 70, 307–316. https://doi.org/10.1016/j.appgeo.2009.06.004.
Kehrman, R.F., 1980. Development of a shallow penetration acoustic reflection technique for mining geology. Final Report Contract No. HO262007: Westinghouse Electric Corporation 178.
Kumpulainen, R.A., Mansfeld, J., Sundblad, K., 1996. Stratigraphy, Age, and Sm-Nd Isotope Systematics of the Country Rocks to Zn-Pb Sulphide Depsoits, Åmmeberg District, Sweden. Econ. Geol. 91, 1009–1021.
Malehmir, A., Bellefleur, G., 2010. Reflection seismic imaging and physical properties of base-metal and associated iron deposits in the Bathurst Mining Camp, New Brunswick, Canada. Ore Geol. Rev. 38, 319–333.
Malehmir, A., Durrheim, R., Bellefleur, G., Urosevic, M., Juhlin, C., White, D.J., Milkereit, B., Campbell, G., 2012a. Seismic methods in mineral exploration and mine planning: A general overview of past and present case history and a look into the future. Geophysics 77, WC173–WC190. https://doi.org/10.1190/geo2012-0028.1.
Malehmir, A., Juhlin, C., Wijns, C., Urosevic, M., Valasti, P., Koivisto, E., 2012b. 3D reflection seismic imaging for open-pit mine planning and deep exploration in the Kevitsa Ni-Cu-PGE deposit, northern Finland. Geophysics 7, WC95–WC108. https://doi.org/10.1190/geo2011-0468.1.
Malehmir, A., Bellefleur, G., Koivisto, E., Juhlin, C., 2017a. Pros and cons of 2D vs 3D seismic mineral exploration surveys. First Breaks 35, 49–55.
Malehmir, A., Maries, G., Bäckström, E., Schön, M., Marsde, P., 2017b. Developing cost-effective seismic mineral exploration methods using a landstreamer and a drophammer. Sci. Rep. 7.
Malehmir, A., Tryggvason, A., Wijns, C., Koivisto, E., Lindqvist, T., Skyttä, P., Montonen, M., 2018. Why 3D seismic data are an asset for exploration and mine planning? Velocity tomography of weakness zones in the Kevitsa Ni-Cu-PGE mine, northern Finland. Geophysics 82, B33–B46. https://doi.org/10.1090/geo2017-0225.1.
Malehmir, A., Manzi, M., Draganov, D., Weckmann, U., Auken, A., 2020. Introduction to the special issue on "Cost-effective and innovative mineral exploration solutions". Geophys. Prospect. 68, 3–6. https://doi.org/10.1111/1365-2478.12915.
Malehmir, A., Markovic, M., Marsden, P., Gil, A., Buske, S., Sito, L., Bäckström, E., Sadeghi, M., Luth, S., 2021. Sparse 3D reflection seismic survey for deep-targeting iron oxide deposits and their host rocks, Ludvika Mines, Sweden. Solid Earth 12, 483–502.
Manzi, M., Gibson, M., Hein, K., King, N., Durrheim, R., 2012. Application of 3D seismic techniques to evaluate ore resources in the West Wits Line goldfield and portions of the West Rand goldfields, South Africa. Geophysics 77, WC163–WC171.
Manzi, M., Cooper, G., Malehmir, A., Durrheim, R., 2019. Improved structural interpretation of legacy 3D seismic data from Karee platinum mine (South Africa) through the application of novel seismic attributes. Geophys. Prospect. 68, 145–163. https://doi.org/10.1111/1365-2478.12900.
Markovic, M., Maries, G., Malehmir, A., von Ketelhodt, J., Bäckström, E., Schön, M., Marsden, P., 2019. Deep reflection seismic imaging of iron-oxide deposits in the Ludvika mining area of central Sweden. Geophys. Prospect. 68, 7–23. https://doi.org/10.1111/1365-2478.12855.
Milkereit, B., Eaton, D., 1998. Imaging and interpreting the shallow crust. Tectonophysics 285, 5–18. https://doi.org/10.1016/S0040-1951(97)00251-5.
Place, J., Malehmir, A., Högdahl, K., Juhlin, C., Nilsson, K., 2015. Seismic characterization of the Grängesberg iron deposit and its mining-induced structures, central Sweden. Interpretation 3, SY41–SY56.
Ruskey. F., 1981. High resolution seismic methods for hard rock mining: In premining investigations for hardrock mines: Proceedings U.S. Bureau of Mines Technology Transfer Seminar, 4–28.
Singh, B., Malinowski, M., Hloušek, F., Koivisto, E., Heinonen, S., Hellwig, O., Buske, S., Chamarczuk, M., Juurela, S., 2019. Sparse 3D Seismic Imaging in the Kylylahti Mine Area, Eastern Finland: Comparison of Time Versus Depth Approach. Minerals 9, 1–22. https://doi.org/10.3390/min9050305.
Schmidt, G., 1959. Results of underground seismic reflection investigations in siderite district of the Siegerland. Geophys. Prospect. 7, 287–290. https://doi.org/10.1111/gpr.1959.7.issue-3.
Schmidt, M., 2019. Scarcity and environmental impact of mineral resources – An Old and Never Ending Discussion. Resources 8, 1–12. https://doi.org/10.3390/resources8010002.
Stephens, M.B., Ripa, M., Lundström, I., Persson, L., Bergman, T., Ahl, M., Wahlgren, C. H., Persson, P.O., Wickström, L., 2009. Synthesis of the bedrock geology in the region, Fennoscandian Shield, south-central Sweden. Geological Survey of Sweden, Ba 58, 259.
Tryggvason, A., Malehmir, A., Rodriguez-Tablante, J., Juhlin, C., 2006. Reflection seismic investigations in the Western Part of the Paleoproterozoic VHMS-Bearing Skellefte District, Northern Sweden. Econ. Geol. 101, 1039–1054.
Urosevic, M., Campbell, A.J., Dahlaus, L., Gendrin, A., Leaney, W.S., Tcherkashnev, S., Verliac, M., 2009. Seismic Monitoring and Verification for the CO2CRC Otway Basin Project, Part 2: acquisition and analysis of borehole seismic data. Energy Procedia 1, 3135–3140. https://doi.org/10.1016/j.egypro.2009.02.095.
Zhao, L., Guangrong, Z., Chen, W., Peng, Y., Xie, B., Peng, X., Zhou, Q., Zeng, Y., 2018. Key seismic survey technologies for deep complex geological structures: A case study of the northern section of the Longmenshan Fault Fold Belt in the Sichuan Basin. Nat. Gas. Ind. B5, 360–370. https://doi.org/10.1016/j.ngib.2018.01.010.
Zepf, V., Reller, A., Rennie, C., Ashfield, M., Simmons, J., 2014. Materials Critical to the Energy Industry. An Introduction (second ed.), BP (2014) London, United Kingdom.
Wu, J., Milkereit, B., Boerner, D., 1995. Seismic imaging of the enigmatic Sudbury structure. J. Geophys. Res. 100, 4117–4130.